Nuclear Engineering and Design 287 (2015) 1–10

Contents lists available at ScienceDirect

Nuclear Engineering and Design

journal homepage: www.elsevier.com/locate/nucengdes

CFD simulations in the nuclear containment using the DES turbulence models

Peng Ding[a], Meilan Chen[c], Wanai Li[b,*], Yulan Liu[a], Biao Wang[b]

[a] School of Engineering, Sun Yat-Sen University, Guangzhou, China
[b] Sino-French Institute of Nuclear Engineering & Technology, Sun Yat-Sen University, Guangzhou, China
[c] China Nuclear Power Technology Research Institute, Shenzhen, China

HIGHLIGHTS

- The k-ε based DES model is used in the nuclear containment simulation.
- The comparison of results between different turbulent models is obtained.
- The superiority of DES models is analyzed.
- The computational efficiency with the DES turbulence models is explained.

ARTICLE INFO

Article history:
Received 17 October 2014
Received in revised form 3 February 2015
Accepted 8 February 2015

ABSTRACT

Different species of gases would be released into the containment and cause unpredicted disasters during the nuclear severe accidents. It is important to accurately predict the transportation and stratification phenomena of these gas mixtures. CFD simulations of these thermal hydraulic issues in nuclear containment are investigated in this paper. The main work is to study the influence of turbulence model on the calculation of gas transportation and heat transfer. The k-ε based DES and other frequently used turbulence models are used in the steam and helium release simulation in THAI series experiment. This paper will show the superiority of the DES turbulence model in terms of computational efficiency and accuracy with the experimental results, and analyze the necessities of DES model to simulate the large-scale containment flows with both laminar and turbulence regions.

1. Introduction

During severe nuclear core-melt accidents, large amount of steam and hydrogen can be released into the air filled containment of nuclear reactors. Flammable mixtures may cause hydrogen combustion which threatens the integrity of Nuclear Power Plant (NPP) containments. In the most recent Fukushima Daiichi nuclear disaster, hydrogen release and explosion are the major cause of the containment breakdown. Therefore, an efficient and accurate prediction of hydrogen distribution in the containment is completely meaningful.

The ex-vessel thermal hydraulic phenomena in the severe accidents have been investigated by the methods of both experiments and numerical calculations during the last several decades. This kind of phenomena contains mass and heat source, heat and mass transfer, pressurization or depressurization, gas transportation and phase transition (Agency, 2008). The steam and hydrogen release that belongs to the multi-component flows contains jet flows with high Reynolds number, plume flows with buoyancy effect and laminar flows. In other words, the large spatial scale in the containment would induce the intense flow close to the release location and the nearly stagnant flow in the far-field (Heitsch et al., 2010). Experiments are performed to study such complicated flows. In early 1970s fuel rod melting experiments were investigated in Soviet Union Kurcharov Institute leading severe accident research. Besides, international standard problem (ISP) related to the Nuclear Energy Agency (OECD/NEA) is made available to the aim of better understanding of containment thermal-hydraulics (Sonnenkalb and Poss, 2009). To demonstrate the actual capability of numerical methods which are used to predict the hydrogen distribution in nuclear containment under severe accident condition, ISP-47 performed a series of experiments, including TOSQAN ($7\,m^3$), THAI ($60\,m^3$) and PANDA ($200\,m^3$) (Bury et al., 2012). In particular, the experiments on German THAI facility addressed the

* Corresponding author at: Sino-French Institute of Nuclear Engineering & Technology, Sun Yat-Sen University, Tangjiawan, Xiangzhou, Zhuhai 519082, China. Tel.: +86 181 02523822; fax: +86 20 87110164.
E-mail address: liwai@mail.sysu.edu.cn (W. Li).

http://dx.doi.org/10.1016/j.nucengdes.2015.02.021
0029-5493/

validation of computer code in a complex and more realistic multi-compartmented geometry. These experiments offer abundance of valuable data for the validation of numerical simulations in NPP containments.

The numerical tools for containment simulations have undergone development for a few decades (Agency, 2008), e.g., US codes MAAP (Henry and Plys, 1990), MELCOR (Gauntt et al., 1998) and COCOSYS (Allelein et al., 2008), European codes GASFLOW (Travis et al., 1998) and ASTEC (Allelein and Jacq, 1999), Russian codes RATEG/SVECHA (Bezlepkin et al., 2004). For computer simulation to predict hydrogen release and distribution in nuclear engineering field, there are two popular methods, lumped-parameter (LP) and CFD codes. Houkema et al. (2008) illustrated that the CFD software CFX-4 was recommended to analyze the containment thermal-hydraulic phenomenon after comparisons with ISP47 experimental data. Allelein et al. (2008) provided the validation of COCOSYS code using the THAI facility experiments which considered hydrogen distributions, recombiner behaviors and aerosol and iodine issues. Royl et al. (2006) calculated the steam and hydrogen distribution with the GASFLOW CFD code and showed very good agreement with experimental results.

When simulating injections in the containment using CFD code, the turbulence model play an important role on the calculation of gas transportation, heat conductivity and diffusion. Some numerical simulations about this phenomenon have been performed employing algebraic or two equation turbulence models. Sha et al. (2004) investigated large-scale containment cooling system test with the k-ε model and showed a good agreement with experimental data. Andreani et al. (2008) drew some conclusions in the ECORA project for the basic assessment of CFD codes, one of which was that the two equation models for turbulence produced much better results than Prandtl's mixing length model. The different flow patterns existing in the steam and hydrogen release, such as jet flow and plume flow, are closely related to turbulence effect in considering the inertia and buoyancy force. Whereas Xiao and Travis (2013) discussed the impacts of different turbulent models on simulation of injections, and showed that the k-ε model tended to over-predict the mixing in the field far away from the jet flow source where the laminar model was more accurate and time-saving. Different turbulence models are required for different flow patterns, which brings difficulties in the calculations of containment flows.

Inside the large-scale containment, flows varying from laminar to turbulence are all existing. The high-Reynolds number turbulence model, e.g., k-ε model, has no mechanism to predict all these phenomena. The low-Reynolds number turbulence model is reported to predict the transition in some degree (Biswas and Fukuyama, 1994), but very fine grids are needed in the boundary layer which is unaffordable for the large-scale spatial problem. The DES approach is reported to be in better agreement with experimental results than unsteady RANS model in predicting transient effects of turbulent separated flows (Benim et al., 2008; Tutar and Holdø, 2001). This paper tries to address the availability of k-ε based DES turbulence models using a series of experiments at the THAI facility. In the numerical simulation, the k-ε based DES model is provided to calculate the heat and mass transfer, gas transportation by updating the new viscosities and diffusion coefficients. This paper will show the superiority of the DES model over other models in computing complicated flows inside the large-scale containment.

2. Computational model

The GASFLOW code (Travis et al., 1998) is a well-tested CFD code for predicting gases transportation in nuclear reactor containment and provides the basis solver for implementing the DES turbulence model. The code employs a second order finite-volume scheme on a structured 3D computational mesh. It solves the unsteady compressible Reynolds averaged Navier–Stokes (RANS) equations using the ICE'D ALE approach (Travis et al., 1998) that consists of three operating steps. The first step is an explicit Lagrangian phase for updating source terms and diffusion terms. The second step is an implicit pressure iteration process to achieve convergence. The last step is named by "Rezone phase" which uses an upwind scheme to calculate the convective terms. There are two coordinate systems for the structured grids, i.e., rectangular system and cylindrical system. The mass and heat transfer inside the boundary layer will be considered using the empirical relations (Bird et al., 2007).

To calculate the turbulent flows in the nuclear containment, the low-Reynolds turbulent model takes much more time than the high-Reynolds one for the resolving of boundary layer on a large area of wall boundary.

In fact, the turbulent boundary condition does not affect the distributions of gas mixture much. Thus wall function is used as the wall boundary treatment for the turbulent model. Besides the already implemented zero equation algebraic and turbulence models in GASFLOW, a new turbulent model called k-ε based DES model is described in the following subsections.

2.1. The standard k-ε turbulence model

As the most popular two-equation model, the k-ε model is applied in the thermal-hydraulics simulation for the NPP containment by many nuclear researchers. The standard k-ε model (Launder and Spalding, 1974) applies turbulent kinetic energy k and dissipation rate ε equations to define turbulent kinematic viscosity ν_t. The equations are given by

$$\begin{cases} \dfrac{\partial(\rho k)}{\partial t} + \nabla\cdot(\rho k\mathbf{U}) = \nabla\cdot\left[\left(\mu_l + \dfrac{\mu_t}{\sigma_k}\right)\nabla k\right] + P_k + P_{kb} - \rho\varepsilon \\ \dfrac{\partial(\rho\varepsilon)}{\partial t} + \nabla\cdot(\rho\varepsilon\mathbf{U}) = \nabla\cdot\left[\left(\mu_l + \dfrac{\mu_t}{\sigma_\varepsilon}\right)\nabla \varepsilon\right] + C_{\varepsilon 1}\dfrac{\varepsilon}{k}(P_k + P_{kb}) - C_{\varepsilon 2}\rho\dfrac{\varepsilon^2}{k} \end{cases} \quad (1)$$

where σ_k, σ_k, $C_{\varepsilon 1}$, $C_{\varepsilon 2}$ are constants, ρ and $\mathbf{U}$ represent the fluid density and velocity respectively. The kinetic source terms P_k and P_{kb} represent turbulence generation due to the viscous forces and the buoyancy respectively.

2.2. The k-ε based DES turbulence model

The first version of DES (Spalart, 1997, also called SA-DES) combines the advantages of RANS in boundary layers and LES elsewhere. By changing the length scale from the RANS scale (the nearest distance to the wall) to the LES scale, the Spalart's SA-DES model changes from the Spalart–Allmarus model to the Smogorisky-like DES model (Spalart, 2009). Since no boundary layer is provided in high-Reynolds turbulence model, the length scale is replaced by the turbulence scale and we can write the k-ε based turbulence model as

$$l_{DES} = \min(l_{RANS}, l_{LES}), \quad (2)$$

where l_{RANS} and l_{DES} are the RANS and LES filter length scales respectively. The RANS length scale is evaluated using dimensional analysis and the LES length scale is the maximum size in the local grid, i.e.,

$$l_{RANS} = \frac{k^{3/2}}{\varepsilon}, \qquad l_{LES} = C_{DES}\max(\Delta x,\ \Delta y,\ \Delta z) \quad (3)$$

where C_{DES} is a constant value of 0.65 used in the DES model. Thus the corresponding dissipative source term used for DES can be rewritten as

$$D_k^{k-\varepsilon} = \frac{\rho k^{3/2}}{l_{DES}} \tag{4}$$

Then the turbulent kinetic energy equation is given by

$$\frac{\partial(\rho k)}{\partial t} + \nabla \cdot (\rho k \mathbf{U}) = \nabla \cdot \left[\left(\mu_l + \frac{\mu_t}{\sigma_k} \right) \nabla k \right] + P_k + P_{kb} - D_k^{k-\varepsilon}, \tag{5}$$

while the equation for the dissipation rate remains the same as the second equation of (1). Comparing to the standard k-ε model, the dissipation rate of turbulence kinetic energy would be increased. Thus the growth of kinetic energy will be constrained and decrease the viscosity of turbulence comparing to the standard k-ε turbulence model.

2.3. Wall function

The shear stress τ_s on the wall boundary can be evaluated using the wall friction velocity u_*,

$$\tau_s = \rho u_*^2. \tag{6}$$

And the wall friction velocity can be calculated using the log-law velocity profile (Travis et al., 1998) inside the boundary layer,

$$\frac{|\mathbf{u}_c|}{u_*} = A \cdot \ln\left(\frac{y_c u_*}{\nu} \right) + B \tag{7}$$

where $\mathbf{u}_c$ is cell-centered average velocity, y_c is the distance from the wall to the cell-centered average tangential speed, ν is the gas mixture molecular kinematic viscosity with $A = 2.5$ and $B = 5.5$. These values are all in the first cell on the wall boundary. Eq. (7) needs an iteration to solve u_*, which is inefficient. An alternative way is to use the one-seventh-power law to approximate the log-law, i.e.,

$$\frac{y_c u_*}{\nu} = 0.15 \left(\frac{y_c |\mathbf{u}_c|}{\nu} \right)^{7/8} \tag{8}$$

Substitute Eq. (8) into right-hand-side of Eq. (7) and u_* is solved using

$$\frac{|\mathbf{u}_c|}{u_*} = 2.19 \cdot \ln\left(\frac{y_c |\mathbf{u}_c|}{\nu} \right) + 0.76. \tag{9}$$

When local Reynolds number $y_c |\mathbf{u}_c| / \nu$ is less than 130.7, it is indicated that the first cell near solid walls lies in the laminar sublayer. In this case, Eq. (9) is replaced by the corresponding laminar formula,

$$\frac{|\mathbf{u}_c|}{u_*} = \left(\frac{y_c |\mathbf{u}_c|}{\nu} \right)^{1/2}. \tag{10}$$

2.4. Effective viscosity, mass diffusion and heat conduction coefficients

After the calculation for the turbulence kinetic energy and dissipation rate, it is possible to consider the influence of turbulence on stress, mass diffusion and heat conduction. The turbulence kinematic viscosity ν_t equations is written as

$$\nu_t = C_u \frac{k^2}{\varepsilon}, \mu_t = \rho \nu_t \tag{11}$$

where $C_u = 0.09$. The mass diffusion coefficient of turbulence effect is calculated as

$$k_t = \frac{\mu_t C_p}{Pr_t} \tag{12}$$

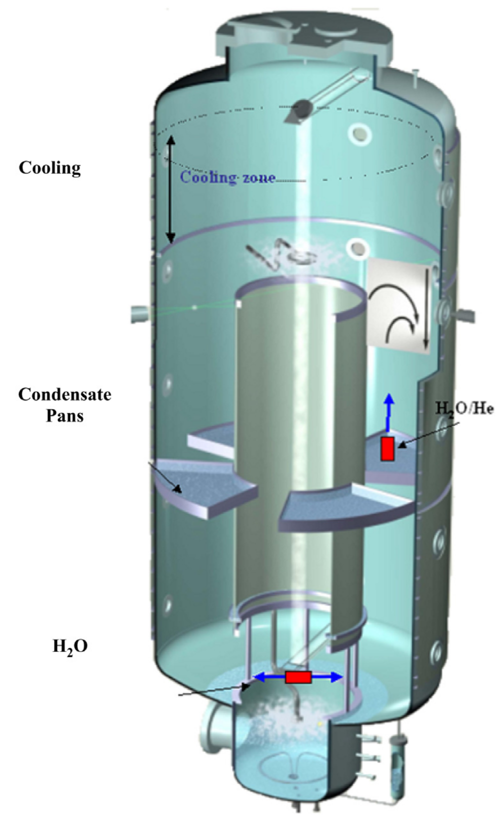

Fig. 1. THAI test vessel and instrumentation (Travis et al., 1998).

The heat conduction considering turbulence is calculated as

$$D_t = \frac{\mu_t}{\rho Sc_t} \tag{13}$$

The final effective kinematic viscosity, mass diffusion and heat conduction coefficients are computed respectively as

$$\nu_{eff} = \nu_l + \nu_t, \quad D_{eff} = D_l + D_t, \quad k_{eff} = k_l + k_t$$

where ν_l, D_l and k_l are the corresponding terms for the laminar case.

3. The THAI experiments and GASFLOW input

The THAI facility is a comprehensive multi-purpose experimental facility which is capable to test thermal hydraulic, aerosol and iodine behavior in containment (Sonnenkalb and Poss, 2009). The facility of volume 60 m^3 has a cylindrical steel vessel with 3.2 m diameter and 9.2 m height. As shown in the vertical cut in Fig. 1, the vessel is divided by an open cylinder of 1.38 m diameter and a horizontal separation plane in the annular region. The separation plane consists of 4 condensate trays with 60° circumference that span from the inner cylinder wall to the vessel wall. The outer cylindrical wall contains three vertical sections with oil heating jackets to maintain steady temperature. According to the built in structures, the facility can be divided into various rooms, which are namely the dome region, the two annular regions between the vessel, the inner cylinder above and below the condensate trays, the central room inside the inner cylinder and the lower plenum below the inner cylinder. A vertical cut through the facility is depicted in Fig. 1. The following subsections 3.2 and 3.3 describe two typical tests in THAI facility, while subsection 3.1 is a standard test case for jet flow.

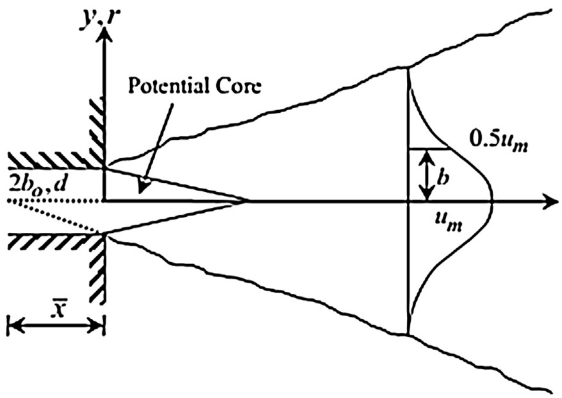

Fig. 2. Problem definition and sketch of free turbulent jet (Aziz et al., 2008).

3.1. Case1: circular jet

The circular turbulent jet case is used to check the capability of the DES model. As shown in Fig. 2, the orifice is 5 mm in diameter and the jet flows from the orifice into the simulated tank of 580 cm width on a side. Tank boundaries are set as smooth and nonslip boundaries and a continuative boundary condition which sets the normal derivatives of all the variables as zero is applied at the outflow section. Details of the circular jet are described by Aziz et al. (2008). The decay of the centerline velocity and the vertical velocity profile for the circular jet are given by following equations,

$$\begin{cases} \dfrac{u_m}{u_0} = \dfrac{A_1}{\sqrt{x/b_0 + \alpha_1}} \\ \dfrac{u}{u_m} = \exp(-0.693\lambda^2) \end{cases} \tag{14}$$

where the value of 6.3 for A_1 was found to fit the experimental data accurately (Rajaratnam, 1976) and λ is given by r/b. The value of 0.5 cm for b_0 represents half of the nozzle width and α_1 is correction for virtual origin.

3.2. Case2: TH-7

Experiment TH-7 (Royl et al., 2006; Travis et al., 1998) is used to benchmark the capabilities of LP and CFD containment codes for simulating steam injection and distributions. This experiment sequentially performs two steam injections, one from an eccentric vertical nozzle in the upper part and the other from a sloped nozzle in the lower part of the facility as shown in Fig. 3. The test starts from an air filled facility that is initially at room temperature (298 K). In the facility, the plane initial temperature is 298.15 K and the initial pressure is 1.013 bar. Four experiment steps are included in TH-7 test as shown in Fig. 4. Step 1 has an axially upward steam injection in the upper annulus for 2000 s with a rate of 35 g/s from both Nozzle 1 and Nozzle 2. These nozzles locations are shown in Fig. 3. In step 2, the steam source switch to Nozzle 1 only which has a steam rate of 35 g/s for another 2000 s. During step 3, the steam source rate is reduced to 5 g/s for another 2000 s at the same location, namely Nozzle 1. From 6000 s to 8000 s step 4 covers the equilibration phase to achieve some stationary conditions without any injections. It has a circular annulus that defined uniform outflow velocities on the circumference of 9 m/s for the steam injection rate of 35 g/s. As shown in Fig. 3, the pressure is recorded in P1 during the experiment. Measured temperature points, T1 and T2, are located in the middle of the facility.

According to the facility symmetry and the experimental process, half section of the facility model is used for the TH-7 simulation in the cylindrical coordinate. A slice of the three dimensional

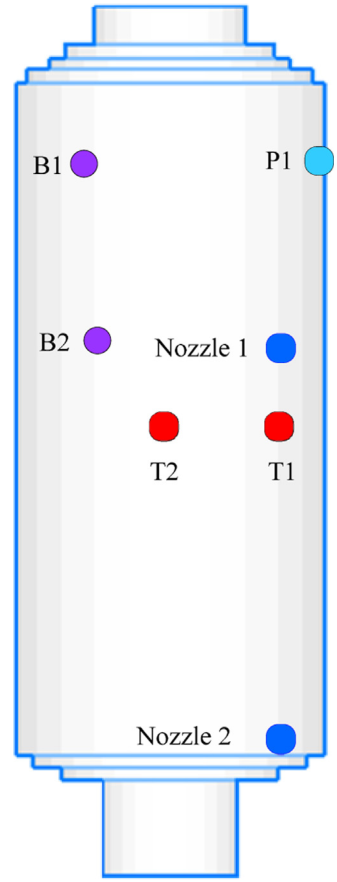

Fig. 3. Localization of nozzles and measuring points in TH-7 experiment.

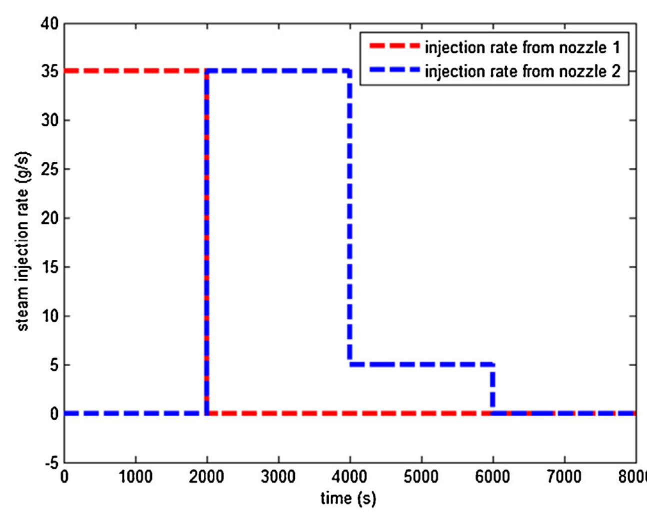

Fig. 4. Steam injection rate for TH-7 experiment.

structured mesh is shown in Fig. 5. This model consists of 38,115 elements.

Also, the mesh spacing is approximately uniform in the boundary layers of the viscous walls. The first cell spacing above the wall is set 0.15 m to predict a logarithmic velocity profile and turbulence quantities outside the viscous sublayer where $y+$ ranges from 1.0 to 50. The mass boundary conditions are used in the nozzles with 0.1 m size elements and the nonslip solid wall conditions are applied in this facility walls. Physical properties of the gas and

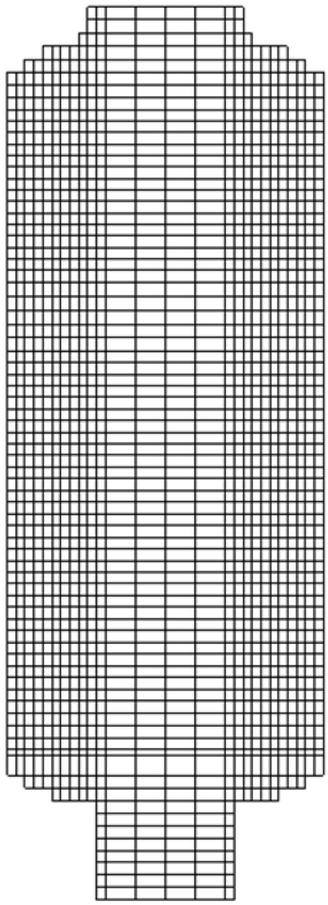

Fig. 5. Mesh for THAI facility simulation.

Table 1
Gas physical properties in the facility and boundary for TH-7.

Properties	Air	Steam
Temperature (K)	298.15	442.11
Pressure (Pa)	1.036×10^5	8.00×10^5
Mole weight	28.85	18.01

steam in the TH-7 case are given in Table 1 with corresponding Prandtl number Pr = 0.7 and Schmidt number $S_c = 0.45$.

3.3. Case 3: TH-13

In the OECD International Standard Problem (ISP-47), experiment TH-13 is also the benchmark of containment codes. With the aim at investigating thermos-hydraulics phenomena about helium and steam injection, four experimental processes are performed. Before the injection, the atmospheric condition in test facility is filled by air with 21 °C and 1.016 bar. As shown in Fig. 7, vertical helium releases into the facility with about 1.625 mole/s injection rate from Nozzle 1 for first 2700 s. Step 2 has an eccentric vertical steam release at about 1.8 mole/s for 2000 s from Nozzle 2. In the third step, a horizontal steam releases from the low location nozzle whose rate is about 1.80 m/s and step 4 is regarded as an equilibration phase without future injections. The locations of nozzles are shown in Fig. 6 (left) and the injection sources are shown in Fig. 7 during the TH-13 experiment. The measured points are identified in Fig. 6 (right). Points from T1 to T7 represent temperature measured points and points from H1 to H3 represent the helium concentration measured points. The measured point B2 is used for the steam concentration. The gas physical properties and boundary pressure

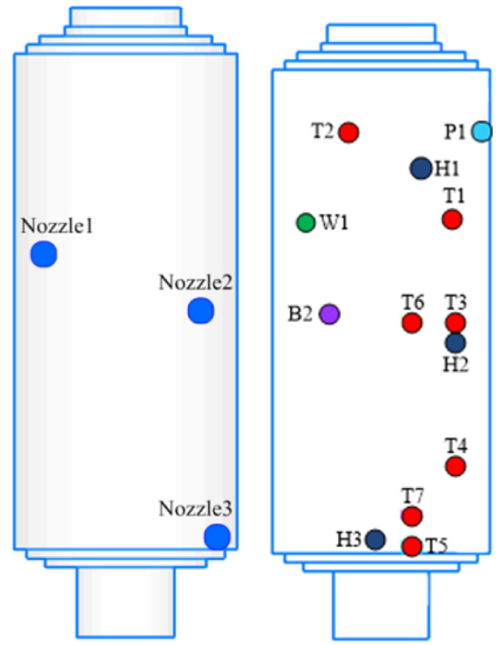

Fig. 6. Localization of nozzles and measuring points for TH-13 experiment.

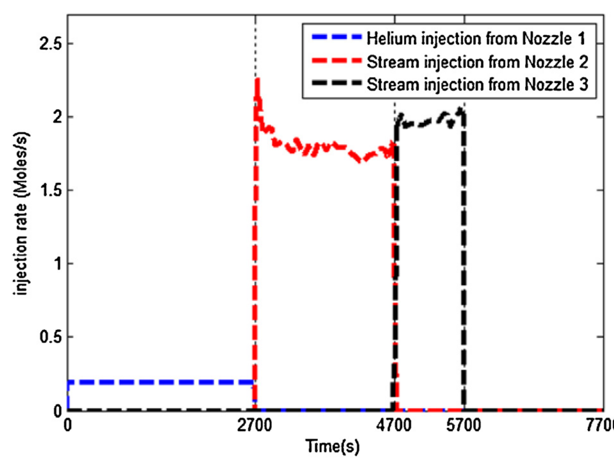

Fig. 7. Helium and steam injection rate for TH-13 experiment.

Table 2
Gas physical properties in the facility and boundary for TH-13.

Properties	Air	Steam	Helium
Temperature (K)	298.75	311.10	302.30
Pressure (Pa)	1.036×10^5	1.036×10^5	1.016×10^5
Mole weight (g/mol)	28.85	18.01	4.00

for different stages of injections can be seen in Table 2 with the same Prandtl and Schmidt number in TH-7 experiment.

Like case TH-7, half segment of the facility is modeled in cylindrical coordinates. This model contains 18,326 elements. All planes are treated as walls in the simulation and the wall function is applied to the boundary layers of the viscous flows. Approximately uniform mesh size near the walls is 0.3 m and the element size of injection boundary is about 0.1 m. To obtain accurate convective terms, the second order van Leer advection scheme is used. The adaptive time stepping feature is used in this case with time step between 1.0e−4 and 0.1 s. This setting can ensure that the maximum residuals of pressure value converged to 10^{-5}.

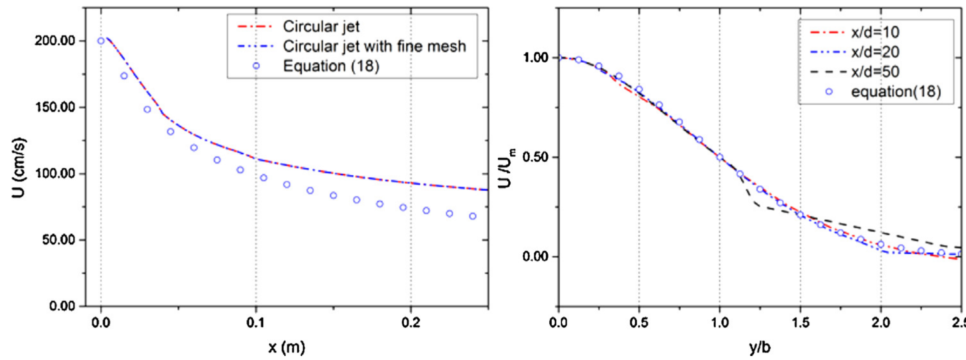

Fig. 8. Profile of centerline velocity decay and vertical velocity of circular jet.

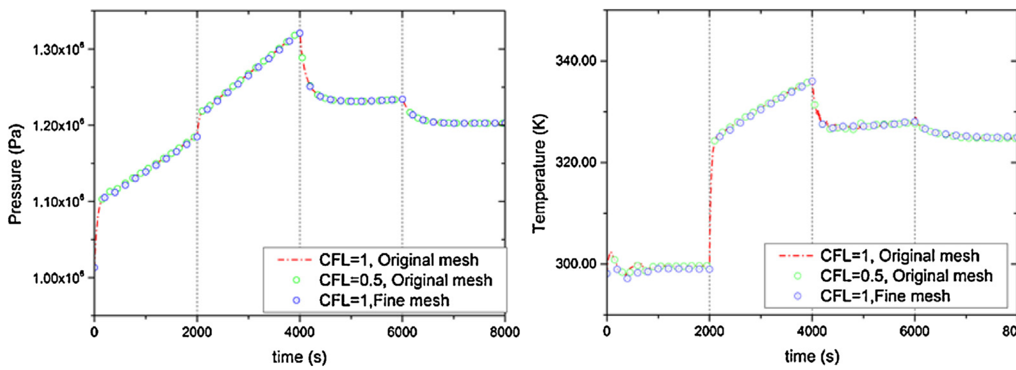

Fig. 9. Time history of pressure (P1) and temperature (T1) for TH-7 with different meshes and CFL numbers.

4. Result and discussion

The numerical simulation presented in this section is used for the evaluation of different turbulence models for injections in the large-scale containment. These models are the k-ε based DES model, the standard k-ε model, the zero-equation algebraic model (zero-equation-alg) and the laminar model. Details of zero-equation-alg model can be seen in Xiao and Travis (2013). The injection cases consist of turbulence flow region and laminar flow region in the large-scale computational domain. Large separation regions or steam diffusion regions far away from nozzles is inappropriate to apply RANS models. Here the DES model together with the wall function described in Section 2 is adopted in this section to switch between different turbulent models in different regions. To satisfy the containment experimental demands in simulations, heat and mass transfer models are added to consider the steam condensation on the surface of slabs and walls. Before the discussion, the global time step calculation should be given for transient flows, i.e.,

$$\Delta t = \mathrm{CFL} \cdot \min(\Delta t_{convection},\ \Delta t_{diffusion}) \tag{15}$$

where CFL is chosen to be 1 when not specified. In this equation, the time step is constrained by both convective and diffusion time steps which are defined by

$$\Delta t_{convection} = \frac{1}{4 \cdot \max\{|u_i|/\Delta x_i,\ |v_i|/\Delta y_i,\ |w_i|/\Delta z_i\}} \tag{16}$$

and

$$\Delta t_{diffusion} = \frac{1}{4 \cdot \lambda_i \cdot ((1/\Delta x_i^2) + (1/\Delta y_i^2) + (1/\Delta z_i^2))},$$

$$\lambda_i = \max\left\{D_{eff,i},\ \nu_{eff,i},\ \left(\frac{k_{eff}}{\rho \cdot c_p}\right)_i\right\} \tag{17}$$

respectively.

4.1. Turbulent circular jet case

For the circular jet, decay of the centerline longitudinal velocity, vertical velocity profiles across the jet are compared with experimental data and accepted empirical equations. In jet flow, viscous effect along the shared interface between the injection regions and outer regions result in the formation of a shear layer that transfer momentum between regions. The shear layer grows with distance to the nozzle. As shown in Fig. 8, results with the DES97 model have good agreement with the empirical Eq. (14), which illustrates that the DES97 model is of accurate implementation.

4.2. TH-7 case

A grid and time convergence study on pressure and temperature measure is performed firstly. The original mesh used for analysis below is shown in Fig. 5, while a fine mesh with half the grid size on every dimension is used for comparison. Three cases are calculated with the DES model, the first one is original mesh with CFL number of 1, the second is original mesh with CFL number of 0.5 and the third is fine mesh with CFL number of 1. The measured pressure and temperature with respect to time are shown in Fig. 9. The figure shows that the measured results of all these three cases are very close, which indicates that original mesh with CFL of 1 is sufficient to compute the pressure and temperature.

For the pressure measured point (P1) above Nozzle 1 shown in Fig. 3, the pressure comparison between calculations with various turbulence models and experimental data is shown in Fig. 10. Due to the faster injection rate from nozzles, pressure in point P1 is significantly affected by the jet flow from Nozzle 1. Along the time evolution shown in Fig. 10, the laminar model gives much lower pressure and the zero-equation-alg model gives much higher one comparing to experimental data for the four steps. The k-ε model fits much better with experiment, while DES series fits the best. For the temperature measured results at points T1 and T2, the

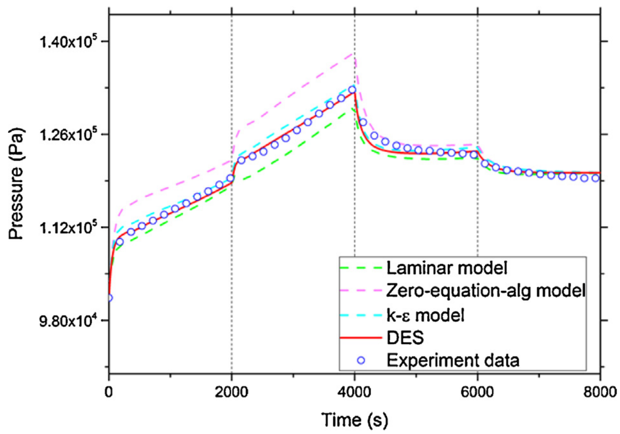

Fig. 10. Time history of pressure for P1 in steam jet flow with different methods in TH-7 calculation.

computational results are shown in Fig. 11. Comparing to experimental results, the laminar models gives an oscillatory curve and smaller values especially on steps 2 and 3 where injections affect these two points strongly. The zero-equation-alg model gives larger values on step 2 and the k-ε model gives much larger values than the experiment. The DES model comes much closer to experimental data for the four steps. The different behaviors of these models and the more accurate results given by the DES model will be analyzed below.

The laminar model will largely under-predict the effective dynamics viscosity, heat and mass conduction coefficients without considering the turbulence effect. The role of the shear stress associated with the dynamics viscosity is to dissipate the kinetic energy into internal energy. When the dynamics viscosity is low, the energy will be accumulated and cause the oscillations as shown in Fig. 11. On the other hand, the diffusion speed associated with heat and mass transfer is low and results in a slower transfer of hot steam coming out from the nozzles. Thus the temperature is much lower than experimental data also shown in Fig. 11. The corresponding pressure is also lower according to the equation of state, which is the facts shown in Fig. 10.

For the zero-equation-alg and k-ε models, a typical point-in-time of 1000 s of step 1 is chosen to plot the viscosity contours using different turbulence models, as shown in Fig. 10. One can find that dynamics viscosity of k-ε models is the largest near the jet nozzle along the flow path, zero-equation-alg model comes second, DES model comes third and laminar model comes last. Following similar reasons in the above analysis, larger dynamics viscosity would bring about larger heat and mass conduction coefficient, thus more kinetic energy will be dissipated into internal energy and heat and mass transfer is faster. Eventually the temperature and pressure will be larger, which is exactly the case that temperature and pressure of zero-equation-alg and k-ε models are larger

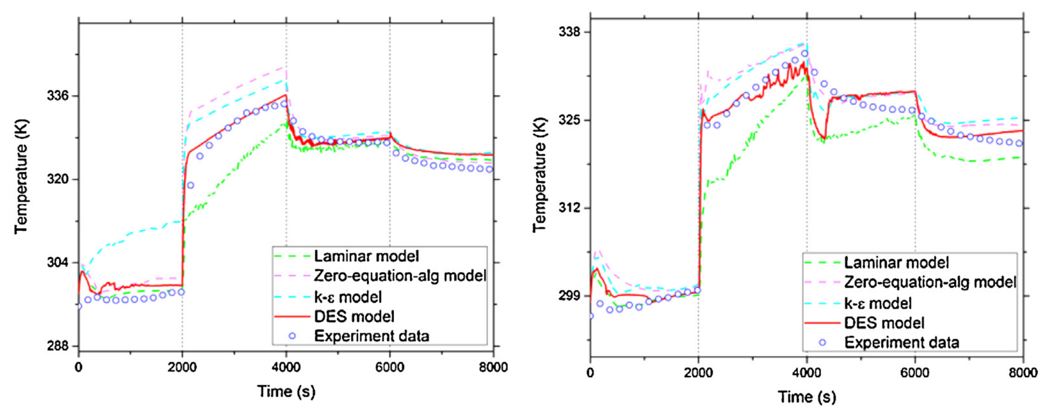

Fig. 11. Time history of temperature for T1 (left) and T2 (right) in steam injection by the method of different turbulence models.

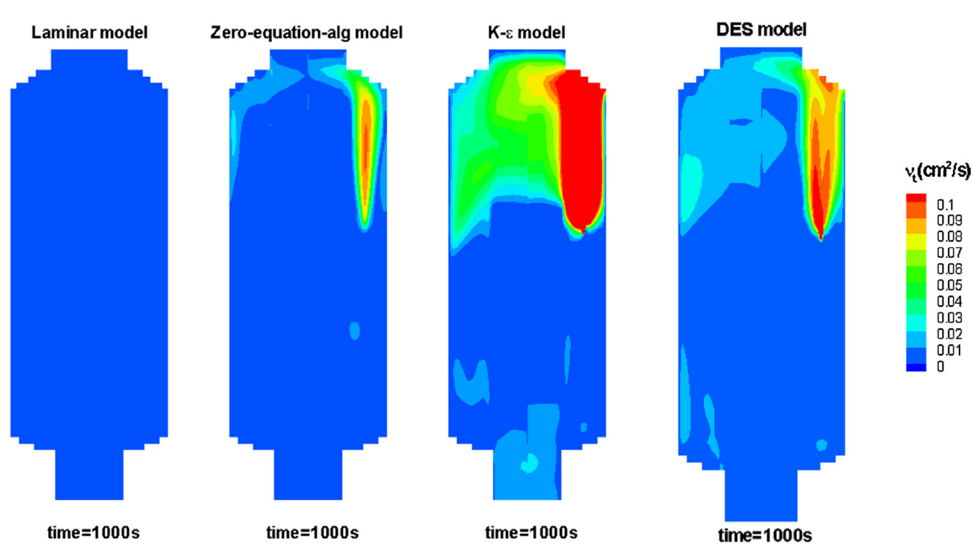

Fig. 12. Comparison of XY-cut of viscosity with different models at time = 1000 s.

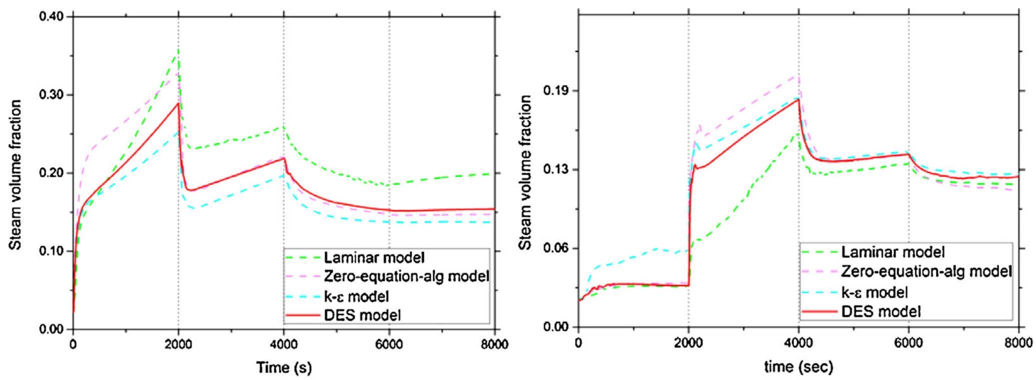

Fig. 13. History of steam fraction at position B1 (left) and B2 (right) for different turbulence models.

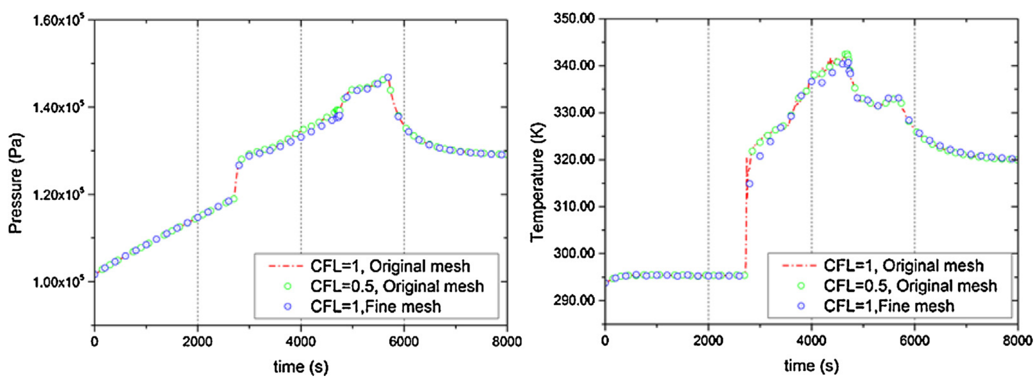

Fig. 14. Time history of pressure (P1) and temperature (T2) for TH-7 with different meshes and CFL numbers.

than experimental ones. In other words, both the zero-equation-alg and k-ε models over-estimate the turbulent viscosity and heat and mass conduction coefficient.

The k-ε based DES model is adopted here to overcome the defects of both pure laminar and k-ε models. For the near jet nozzle regions with coarse grids, the length scale is still the same as the RANS scale and the DES model has the same ability as k-ε model in predicting the viscosity, which reflects in Fig. 12 that the viscosity contour near jet nozzles is the same as k-ε model. For the places away from the nozzle, the smaller DES length scale l_{DES} comparing to l_{RANS} would increase the dissipation source term $D_k^{k-\varepsilon}$ in Eq. (4) for the kinetic equation. Then kinetic energy would decrease faster than k-ε model and it results in smaller viscosity away from the jet nozzle, which can be validated from Fig. 12 by comparing the viscosity between DES and k-ε models.

The turbulence model not only affects the average pressure and temperature, but also affects the concentration of every species greatly according to the mass diffusion coefficient in Eq. (13). As shown in Fig. 13, the concentration of k-ε based DES model lies between the laminar model and k-ε model at both T1 and T2 points, which agrees with that fact that mass conduction coefficients of DES series lies between the other two models. During the first two steps, steam volume distribution increases because of the high steam injection rate. Due to the higher steam temperature, steam fraction is higher in the upper facility than the lower part. In the step 3 and step 4, as shown in Fig. 12, steam fraction decreases because of diffusion and wall condensation effect.

4.3. TH-13 case

The grid and time convergence study is also performed firstly with three cases with the DES model, i.e., original mesh with CFL number of 1, original mesh with CFL number of 0.5 and fine mesh with CFL number of 1. The measured pressure and temperature with respect to time history are shown in Fig. 14. Only slight difference is observed is observed for these three cases.

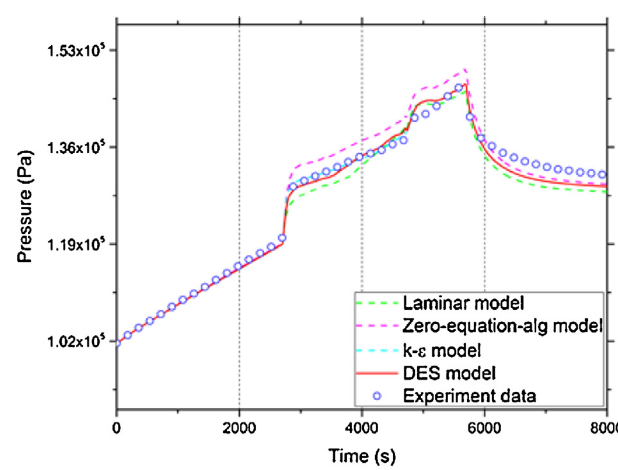

Fig. 15. History of pressure for P1 in TH-13 simulation.

As shown on the left of Figs. 15 and 16, the pressure at point P1 and the temperature at points T1 and T2 calculated with various turbulent models all show the same trend with the experiment and agree with experimental data quite well except the ones with laminar model. Ignoring the turbulent effect increases the pressure prediction at measured point P1 above Nozzle 1 during the second experiment step. The history of temperature at points T1 and T2 is shown on the right of Fig. 16. In spite of the oscillations, the DES model match reasonably well with the experimental measurements. The main reason of the curve oscillation is that the

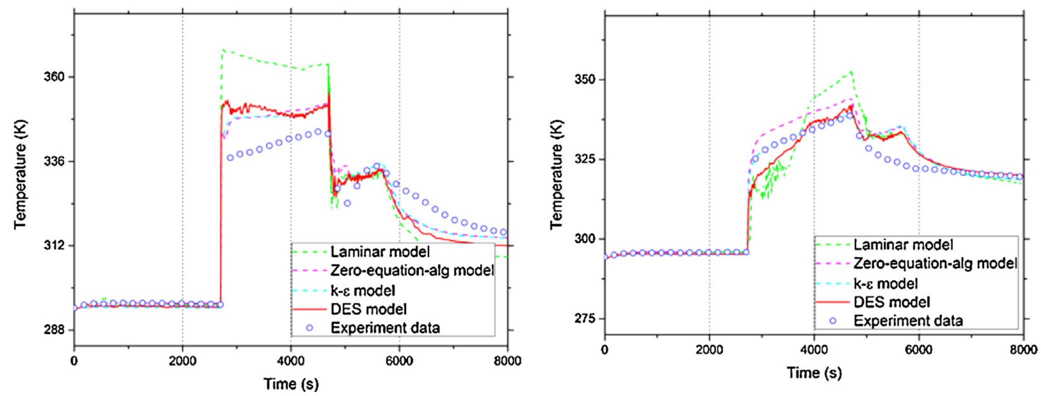

Fig. 16. History of temperature for T1 (left) and T2 (right) in TH-13 simulation.

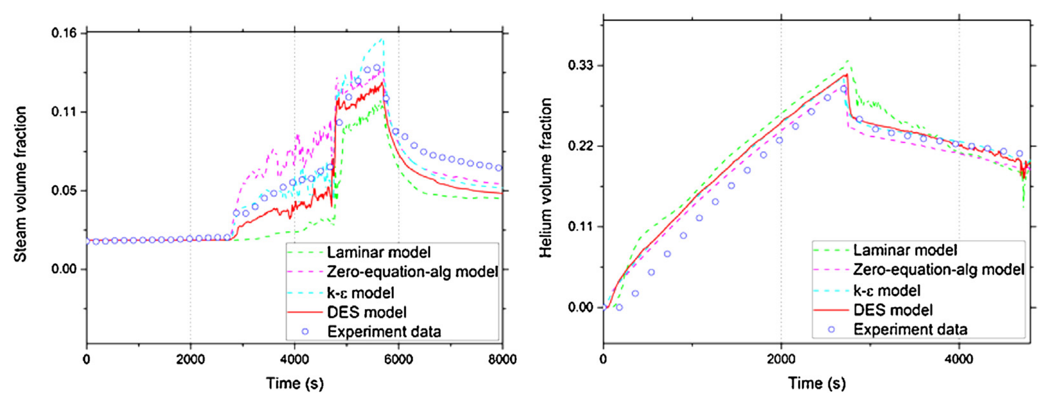

Fig. 17. Comparisons of steam and helium fraction history at B2 and H1 (right) with different models.

coarse grids could not resolve the small scale vortices to dissipate turbulent kinetic energy into internal energy.

The comparison of the steam and Helium concentration with different turbulence models is observed in Fig. 17. The k-ε model and the k-ε based DES model have relatively better agreement with experimental measurements. Fig. 17 (left) shows the laminar model under-predicts the steam volume fraction in H1 above Nozzle 2. This model without turbulent viscosity produces insufficient mass diffusion and lower the steam concentration at point H1. As shown in Fig. 17 (right), the calculations of the helium volume fraction with various turbulent models have a perfection trend comparing with experimental data. The result bias presented is related to some sporadic deviations of initial condition in the case.

Like the case TH-7, the k-ε model and the zero-equation-alg model can produce high turbulent viscosity in the injection region for the case TH-13 as shown in Fig. 18. In the laminar flow region, the k-ε turbulent model would predict too much turbulent viscosity which is inefficient for computational cost. The laminar model ignoring turbulent effect is improperly used in turbulent flow regions for the injection simulation. A clearer transition

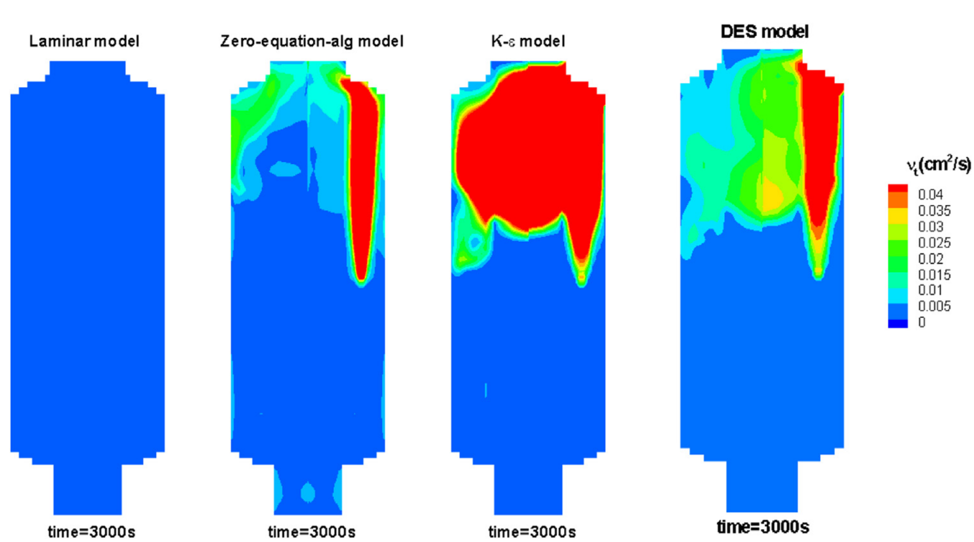

Fig. 18. Comparison of XY-cut of viscosity with different models at time = 3000 s.

Table 3
Comparison of compute cost for TH-7 and TH-13 simulation between different models.

Model	Laminar	Zero-equation-alg	k-ε model	DES
TH-7 case	T_{TH7}	$0.74T_{TH7}$	$1.51T_{TH7}$	$0.56T_{TH7}$
TH-13 case	T_{TH13}	$0.88T_{TH13}$	$1.79T_{TH13}$	$0.79T_{TH13}$

process with DES model can be observed near Nozzle 2 where viscosity is increased gradually. Also in regions away from Nozzle 2 the decrease of the viscosity with DES model shows a clearer and more stratified process comparing to other models.

4.4. Discussion

This work investigates affections of the turbulent models on the injection in a large-scale containment using cases TH-7 and TH-13 in the THAI facility. The injection in these two cases induces a free shear driven flow in a large-scale facility, along with strong mixing of multi-component gases. For the regions near the jet nozzles, the injection produces separation induced turbulence flows which is convection-dominated. Temperature and gas species transport are mainly determined by the mean velocity. Nevertheless, for the regions away from the jet nozzles or long after the jet flows, the kinetic energy is dissipated into internal energy and the turbulence cannot be maintained. The flow will turn laminar and is diffusion dominated. Thus, both the laminar model and the pure RANS turbulence model are not appropriate for all these regions, which is also concluded by Xiao and Travis (2013).

The laminar model is only beneficial to speed up computation in diffusion dominated regions by using smaller viscosity and larger time step according to Eq. (17). In the convective dominated regions, the velocity magnitude of laminar model is larger than that of turbulence model since turbulence model would allow more kinetic energy to dissipate into internal energy, which makes the time step of laminar case smaller than that of turbulence models according to Eq. (16). The global time step in Eq. (15) is restricted by both the convection and diffusion time step. As shown in Table 3 of the CPU time using different models for the two cases, the k-ε model takes more time because it largely overestimates the viscosity and the diffusion time is too small. The zero-equation-alg model costs less than laminar models for it does not give too large viscosity. The DES model which gives the reasonable viscosity takes the least time among all these models.

5. Conclusion

This work investigated influence of different turbulence models on the injection in nuclear containment during the severe accident. These models contained the k-ε based DES model, the standard k-ε model, the zero-equation-alg model and the laminar model. CFD simulations of the TH-7 and TH-13 test cases were performed with various turbulence models in this work. Numerical results in terms of pressure, temperature and species concentration obtained by these turbulence models, are presented and compared with experimental data. This paper shows that the k-ε based DES turbulence model combining both the merits of RANS and laminar models is applicable to the injection issue with coarse grids in a large-scale containment. Comparing to other models, it is more accurate and computationally efficient in the current cases. Also, the superiority of the DES model is analyzed in the convection and diffusion dominated regions. The future work will focus on the calculation on a much finer mesh near the nozzle to study the transition process using DES and its applications for more containment flow cases.

References

Agency, I.A.E., 2008. Approaches and Tools for Severe Accident Analysis for Nuclear Power Plants. International Atomic Energy Agency.

Allelein, H., et al., 2008. COCOSYS: status of development and validation of the German containment code system. Nucl. Eng. Des. 238 (4), 872–889.

Allelein, H.J., Jacq, F., 1999. Severe accident code ASTEC development and validation. In: EUROSAFE Conference, Paris.

Andreani, M., et al., 2008. A benchmark exercise on the use of CFD codes for containment issues using best practice guidelines: a computational challenge. Nucl. Eng. Des. 238 (3), 502–513.

Aziz, T.N., Raiford, J.P., Khan, A.A., 2008. Numerical simulation of turbulent jets. Eng. Appl. Comput. Fluid Mech. 2 (2), 234–243.

Benim, A.C., Pasqualotto, E., Suh, S.H., 2008. Mo0delling turbulent flow past a circular cylinder by RANS, URANS LES and DES. Progr. Comput. Fluid Dyn.: Int. J. 8 (5), 299–307.

Bezlepkin, V.V., et al., 2004. The development of computer codes for the simulation of severe accidents at nuclear power stations I. Therm. Eng. 51 (2), 88–95.

Bird, R.B., Stewart, W.E., Lightfoot, E.N., 2007. Transport Phenomena. John Wiley & Sons.

Biswas, D., Fukuyama, Y., 1994. Calculation of transitional boundary layers with an improved low-Reynolds-number version of the k-ε turbulence model. J. Turbomach. 116 (4), 765–773.

Bury, T., Składzień, J., Fic, A., 2012. Validation of the heat and mass transfer models within a pressurized water reactor containment using the International Standard Problem No. 47 data. Arch. Thermodyn. 33 (2), 23–46.

Gauntt, R.O., et al., 1998. MELCOR Computer Code Manuals. Division of Systems Technology Office of Nuclear Regulatory Research, US Nuclear Regulatory Commission.

Heitsch, M., Baraldi, D., Wilkening, H., 2010. Simulation of containment jet flows including condensation. Nucl. Eng. Des. 240 (9), 2176–2184.

Henry, R.E., Plys, M.G., 1990. MAAP-3.0 B-Modular Accident Analysis Program for LWR Power Plants: User Guide. Electric Power Research Report EPRI NP-7071-CCML, Vols. 1 (2).

Houkema, M., Siccama, N.B., Lycklama À Nijeholt, J.A., Komen, E., 2008. Validation of the CFX4 CFD code for containment thermal-hydraulics. Nucl. Eng. Des. 238 (3), 590–599.

Launder, B.E., Spalding, D.B., 1974. The numerical computation of turbulent flows. Comput. Methods Appl. Mech. Eng. 3 (2), 269–289.

Rajaratnam, N., 1976. Turbulent Jets. Elsevier.

Royl, P., Lee, U.J., Travis, J.R., Breitung, W., Karlsruhe, F., 2006. Benchmarking of the 3D CFD Code GASFLOW II with Containment Thermal Hydraulic Tests from HDR and ThAI.

Sha, W.T., Chien, T.H., Sun, J.G., Chao, B.T., 2004. Analysis of large-scale tests for AP-600 passive containment cooling system. Nucl. Eng. Des. 232 (2), 197–216.

Sonnenkalb, M., Poss, G., 2009. The International Test Programme in the THAI Facility and its Use for Code Validation. EUROSAFE Forum, Brussels, Belgium.

Spalart, P.R., 2009. Detached-eddy simulation. Ann. Rev. Fluid Mech. 41, 181–202.

Travis, J.R., et al., 1998. GASFLOW: A Computational Fluid Dynamics Code for Gases, Aerosols and Combustion. FZKA-5994, Vols. I–III.

Tutar, M., Holdø, A.E., 2001. Computational modelling of flow around a circular cylinder in sub-critical flow regime with various turbulence models. Int. J. Numer. Methods Fluids 35 (7), 763–784.

Xiao, J., Travis, J.R., 2013. How critical is turbulence modeling in gas distribution simulations of large-scale complex nuclear reactor containment? Ann. Nucl. Energy 56, 227–242.